

## Advanced neutron and X-ray techniques for insights into the microstructure of EB-PVD thermal barrier coatings

Anand Kulkarni<sup>a</sup>, Allen Goland<sup>a</sup>, Herbert Herman<sup>a,\*</sup>, Andrew J. Allen<sup>b</sup>, Tabbetha Dobbins<sup>b</sup>,  
Francesco DeCarlo<sup>c</sup>, Jan Ilavsky<sup>c</sup>, Gabrielle G. Long<sup>c</sup>, Stacy Fang<sup>d</sup>, Paul Lawton<sup>d</sup>

<sup>a</sup> State University of New York, Stony Brook, NY 11794, United States

<sup>b</sup> National Institute of Standards and Technology, Gaithersburg, MD 20899, United States

<sup>c</sup> Argonne National Laboratory, Argonne, IL 60439, United States

<sup>d</sup> Chromalloy Gas Turbine Corporation, Orangeburg, NY 10962, United States

Received 5 January 2006; received in revised form 3 March 2006; accepted 20 March 2006

### Abstract

The ongoing quest to increase gas turbine efficiency and performance (increased thrust) provides a driving force for materials development. While improved engine design and usage of novel materials provide solutions for increased engine operating temperatures, and hence fuel efficiency, reliability issues remain. Thermal barrier coatings (TBCs), deposited onto turbine components using the electron-beam physical vapor deposition (EB-PVD) process, exhibit unique pore architectures capable of bridging the technological gap between insulation/life extension and prime reliance. This article explores the potential of advanced X-ray and neutron techniques for comprehension of an EB-PVD TBC coating microstructure. While conventional microscopy reveals a hierarchy of voids, complementary advanced techniques allow quantification of these voids in terms of component porosities, anisotropy, size and gradient through the coating thickness. In addition, the derived microstructural parameters obtained both further knowledge of the nature and architecture of the porosity, and help establish its influence on the resultant thermal and mechanical properties.

© 2006 Elsevier B.V. All rights reserved.

**Keywords:** Thermal barrier coatings; EB PVD; Small-angle neutron scattering; Ultra small-angle X-ray scattering; X-ray microtomography; Microstructure characterization; Porosity–property correlations

### 1. Introduction

Zirconia-based thermal barrier coatings (TBCs) are extensively applied to the hot sections in gas turbine engines and provide protection against thermomechanical shock, high-temperature oxidation and hot corrosion degradation [1–3]. The TBC comprises a two-layer system: an outer insulating ceramic layer and an underlying oxidation-resistant metallic layer (bond coat) deposited directly onto the surface of the metallic component. The top ceramic layer provides benefits in performance, efficiency and durability through (a) increased engine operating temperature; (b) extended metallic component lifetime when subjected to elevated temperature and stress; and (c) reduced cooling requirements for the metallic components [4,5]. The scale, performance and cost requirements determine the choice

for a particular TBC application. The development and acceptance of TBCs are closely linked to processing technology: in this connection, ceramic topcoats are presently deposited using air plasma spray (APS) or electron-beam physical vapor deposition (EB-PVD) processes, which each produce distinctive microstructures. In the case of plasma spray, feedstock powder is melted and accelerated to high velocities, impinging upon the substrate, and rapidly solidifying to form a “splat” (a flattened particle). The deposit develops by successive impingement of the molten particles and inter-bonding among the splats [6,7]. Thus, APS coatings have a splat-based layered structure, which offers advantages over EB-PVD in terms of insulation and cost effectiveness [8]. On the other hand, the EB-PVD process, in which the coating develops by vapor condensation, offers superior strain tolerance and thermal shock resistance, thereby providing significant lifetime enhancements [9,10]. Furthermore, cooling hole closure is avoided and an aerodynamic design of the blades is maintained. However, one disadvantage of EB-PVD coatings arises from its columnar structure, which leads to high thermal

\* Corresponding author. Tel.: +1 516 632 8510; fax: +1 516 632 8052.  
E-mail address: [hherman@ms.cc.sunysb.edu](mailto:hherman@ms.cc.sunysb.edu) (H. Herman).

conductivity compared to that of APS coatings. In this manner, coating microstructure is a significant factor in determining coating behavior during service life [11].

Control of the thermal conductivity and mechanical properties necessitates a comprehensive understanding of the microstructural features in TBCs. Knowledge of the nature, origin and influence on the TBC properties and failure mechanisms of these features, would enable microstructures to be tailored with enhanced reliability for specific applications. Since the microstructure develops by vapor condensation, the influence of processing parameters during deposition, such as the deposition temperature, vapor pressure and substrate conditions have been studied [12]. In the EB-PVD process, vapor is produced by heating the source material with an electron beam, and the evaporated atoms condense onto the substrate. Crystal nuclei are formed on favored sites, growing both laterally and through the thickness to form individual columns, resulting in a high degree of intercolumnar porosity [13,14]. This specific coating structure, with low in-plane Young's modulus, provides more stress relief on thermomechanical loading and can also accommodate misfit stresses resulting from CTE mismatch. Also, since growth depends on competitive processes, which can vary during deposition, variations in microstructure and texture are anticipated throughout the thickness of the coating. This necessitates the need for microstructural insights of possible porosity/microstructure gradients in the coatings.

In this paper, advanced scattering techniques are employed for the microstructural characterization of an EB-PVD TBC. While conventional microscopy (SEM and TEM) studies reveal the nature of the microstructural features in these ceramic coatings, quantitative microstructural information is sought using high-resolution X-ray microtomography (XMT) along with ultra small-angle X-ray scattering (USAXS) and small-angle neutron scattering (SANS). The goal is to obtain insights into the microstructure with respect to porosity, its dimensions and the pore size distributions of open and closed porosity in 3D along with the porosity gradient. These model-based results are compared to results obtained from traditional characterization techniques. Also, thermal and mechanical properties of the coatings were measured to verify the existence of microstructural anisotropy in these systems.

## 2. Experimental

The TBC system<sup>1</sup> investigated was deposited at Chromalloy Gas Turbine Corporation, Orangeburg, NY, and comprises a 800- $\mu\text{m}$  thick EB-PVD 7–8% by mass  $\text{Y}_2\text{O}_3$ -stabilized  $\text{ZrO}_2$  coating (topcoat) on a 50- $\mu\text{m}$  thick NiCoCrAlY coating (bond coat), also deposited by EB-PVD, on a stainless steel substrate. A freestanding form of this coating was used for porosity determinations, thermal conductivity measurements and SANS studies. For USAXS, XMT and elastic modulus measurements,

the coatings were bonded to the substrate. Specimens were sliced using a low-speed diamond saw and then polished using a tripod polisher, to create a nominal cross-sectional sample thickness of 250  $\mu\text{m}$  for X-ray investigations. Phase content and crystallographic texture were determined by X-ray diffraction using  $\text{Cu K}\alpha$  radiation. The strongest diffraction peaks were used to determine the texture of the coating. Morphological features in the microstructure were studied using optical microscopy and scanning electron microscopy (SEM). Thin-foil cross-sections were also studied by cross-sectional transmission electron microscopy (X-TEM). In this case, samples were prepared by slicing and punching a TBC cross-section to obtain a 3 mm diameter disc. This disc was polished and ion milled in a GATAN ion mill at 5 kV and 2 mA. X-TEM was performed with a Phillips CM12 unit, operated at 120 kV with a  $\text{LaB}_6$  filament.

Various aspects of the porosity were measured by different techniques. Surface-connected porosity was measured by means of mercury intrusion porosimetry (MIP) using a Quantachrome Autoscan 33 porosimeter. Even though XMT measures both the open and the closed porosity, the spatial resolution of our current XMT facility limits the detection of the pores to those larger than 0.5  $\mu\text{m}$  in diameter. The most reliable determination of the total porosity content, needed for SANS analysis, was obtained using the precision density (PD) method, where mass-over-volume ratios were obtained for cut rectilinear specimens. In the present case, the fractional density (and hence the total porosity) could be obtained with an uncertainty of standard deviation of  $\pm 0.1\%$ , based on the average of 10 measured identical specimens and an assumed theoretical density of 6  $\text{g}/\text{cm}^3$ .

### 2.1. Thermal and mechanical property measurements

Thermal conductivity measurements were made on a 12.5 mm (0.5 in.) diameter disk, coated with carbon, using a laser-flash thermal diffusivity instrument (Netzsch Corporation\*, Boston, MA) in the out-of-plane direction. Elastic modulus measurements performed by means of depth-sensitive indentation measurements, were carried out with a Nanotest\* 600 instrument (Micromaterials Inc., Cambridge, UK) with a 1.59 mm (1/16 in.) WC-Co spherical indenter with a maximum load of 10 N. Elastic modulus measurements were carried out in three directions (two in-plane and one out-of-plane directions) to examine the anisotropy of the coatings. The instrument enables a basic load/displacement curve to be obtained, or multiple partial load/unload cycles can be performed. This allows hardness and elastic modulus values to be measured as a function of the load/contact stress. The indentation procedure consisted of 10–15 loading/unloading cycles. The load–displacement records were evaluated based on the Oliver and Pharr method [15] where the elastic modulus is determined from the elastic recovery part of the unloading curve.

### 2.2. Small-angle neutron scattering

SANS studies were carried out using the NIST/NSF 30 m NG3 SANS instrument at the Cold Neutron Research Facility at the National Institute of Standards and Technology,

<sup>1</sup> Information on commercial products is given for completeness and does not constitute or imply their endorsement by the National Institute of Standards and Technology.

Gaithersburg, MD. The availability of a flexible measurement geometry on this instrument provides the means to extend multiple SANS analysis of microstructure-related properties to thin coatings, which are more representative of industrial applications. This is the case, provided that sufficiently copious multiple scattering occurs for the MSANS formalism (developed previously) to be valid. In MSANS studies, a monochromatic beam of long-wavelength (cold) neutrons passes through the specimen in transmission geometry and the multiple-scattered beam profile is recorded on a 2D detector. Details of the measurement are described elsewhere [16,17]. The multiple scattering is from the pores and the voids within the coating and is due to a difference in neutron scattering length density between the solid material and the pores. At a shorter neutron wavelength (0.5 nm) single scattering occurs that is associated more specifically with the void/solid interface (Porod scattering). Anisotropic Porod scattering amplifies the anisotropies actually present and enables the different void components to be distinguished due to their different characteristic orientation distribution. However, orientational averaging of the Porod scattering from the sample yields the total void surface area per unit sample volume can be obtained, independent of the precise void morphology. The fine features in the microstructure are major contributors to this deduced surface area. Meanwhile, anisotropic MSANS studies involve a measurement of the anisotropic beam broadening due to multiple scattering at long neutron wavelengths (1–1.8 nm). The multiple scattering usually arises from the coarse features in the microstructure. The MSANS beam broadening ( $r_c$ ) versus wavelength for two sample orientations, with the incident beam out-of-plane (normal to the coating) and in-plane (i.e., in the substrate plane), yields information on the microstructure anisotropy. The sector-averaged anisotropic MSANS data (on the SANS instrument's 2D detector) also provide microstructural orientation information, as discussed in detail elsewhere [17,18].

A complete description of the microstructure is obtained by combining MSANS measurements for different sample orientations, anisotropic Porod surface area distributions, and the total porosity from PD measurements. To acquire a quantitative delineation of three of the main void components (intercolumnar pores, intracolumnar feather-like cracks and globular/elongated pores) in terms of their porosity contributions, dimensionality and orientation distribution, the following four constraints have to be fulfilled in the MSANS analysis:

- (1) The component porosities are consistent with the total porosity obtained using precision density measurements.
- (2) The component surface areas are consistent with the total surface area obtained from anisotropic Porod scattering experiments.
- (3) Model predictions of the circularly averaged MSANS beam broadening versus wavelength are consistent with the experimental data for both orientations: out-of-plane (spray direction) and in-plane (orthogonal direction).
- (4) The derived MSANS anisotropy (perpendicular to the substrate) is consistent with that observed experimentally.

In general, MSANS analysis can provide structural information for void opening dimensions up to around 4  $\mu\text{m}$ .

### 2.3. Ultra small-angle X-ray scattering

Ultra small-angle X-ray scattering (USAXS) studies were carried out on the UNICAT beam line 33-ID at the Advanced Photon Source, Argonne National Laboratory, Argonne, IL. This instrument utilizes Bonse-Hart double-crystal optics [19] to extend the range of SAXS down to lower scattering vectors,  $Q$ , where  $Q = |\mathbf{Q}| = (4\pi/\lambda)(\sin \theta)$  and  $2\theta$  is the scattering angle. With minimum  $Q = 0.0015 \text{ nm}^{-1}$ , the maximum void opening dimension obtainable from the data is around 1.5  $\mu\text{m}$ . In a modified form of the standard USAXS experiment, a finely collimated and highly monochromatic X-ray beam (using horizontal and vertical diffracting crystals) is incident on the specimen in transmission geometry and the scattered intensity is measured. Use of both horizontal and vertical diffracting crystals removes the intrinsic slit-smearing geometry of the standard USAXS experiment. The details of the experiment are described elsewhere [20]. The X-ray energy used was 17 keV, which was selected to penetrate through the highly absorbing YSZ coatings. Due to the short wavelength used and the small sample thickness (typically 200  $\mu\text{m}$ ), the contamination of the results by multiple scattering is relatively small and usually is corrected. Two data collection methods are combined in the present studies. In the first, the scattered intensity is measured as a function of  $Q$  for each orientation of the sample azimuthal angle  $\alpha$ . In the second, the scattered intensity at a fixed  $Q$  is measured as a function of  $\alpha$  by rotating the sample in the beam. Variation in the scattering anisotropies observed at different  $Q$  are associated with the variation in the microstructure anisotropy at different length scales, thus giving a quantitative map as a function of the sizes of the scattering populations.

### 2.4. Computed microtomography

X-ray microtomography (XMT) studies were carried out on the XOR 2-BM beam line at the Advanced Photon Source. The experimental details and setup are described elsewhere [21,22]. In this experiment, a large-area, collimated X-ray beam traverses the sample, and the transmitted X-rays are recorded on an area detector. For the TBC, the thickness was 250  $\mu\text{m}$ , owing to the high attenuation of YSZ material. Images (X-ray attenuation maps) are recorded at discrete angular intervals (typically in  $1/4^\circ$  steps) as the sample is rotated for a total of  $180^\circ$  about the vertical axis perpendicular to the incident X-rays. In addition to the 720 2D attenuation maps, “dark-field” (background measurements with the X-rays off) and “white-field” (X-ray on measurements, with no sample in the beam) images are acquired. These images are necessary for normalizing the 2D projection images. The normalized images are then aligned to ensure that the rotation axis is accurately located at the center of the images. The data are reconstructed using a filtered back-projection algorithm and 2D slices are then stacked to build 3D images of the microstructural features. While the pixel size (image resolution for software thresholding) was 1.3  $\mu\text{m}$ , this does not represent

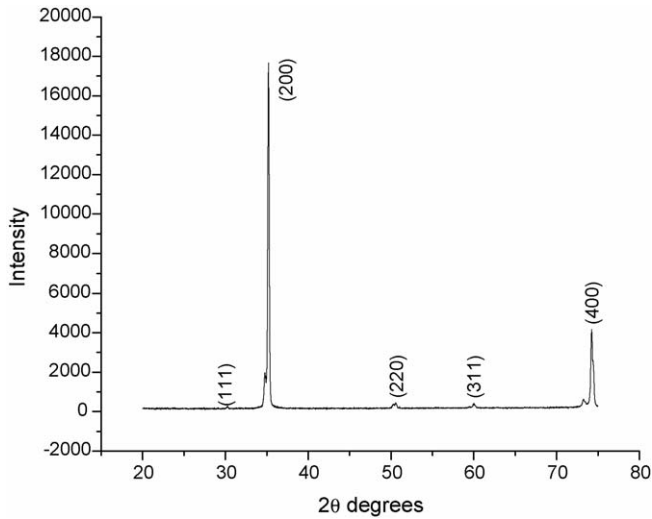


Fig. 1. X-ray analysis shows a non-transformable tetragonal phase structure with a (200) texture.

the minimum pore size that can be resolved. Realistically the pore has to be larger than this size at least in one dimension to be recognizable. The technique provides volumetric information on microstructure distribution by mapping 3D X-ray coefficients through the sample.

For the analysis of the X-ray tomographic data, 3D medial axis transforms are used to obtain quantitative information on porosity and its gradient with thickness [23]. The medial axis transform is a dimensional reduction of an object to its skeletal remnant, preserving information on extent and connectivity of the original object. Intuitively, a medial axis is the skeleton of an object along its geometric middle (a point for a sphere and a line along the center for a cylinder). The analysis involves thresholding an overlapping bivariate mapped distribution of attenuation coefficients (tomographic raw images) to obtain segmented (black and white) images. This is followed by construction of the medial axis with an iterative erosion procedure [24] to trace the fundamental geometry of the void pathways.

### 3. Results and discussions

The primary aim of this investigation was to gain insights into the microstructure of EB-PVD coatings using advanced characterization techniques. This section presents results from the “conventional” microstructural and phase characterization complemented with results from SANS, USAXS and XMT studies. Thermal conductivity and elastic modulus measurements are presented later. X-ray diffraction studies show a single-phase

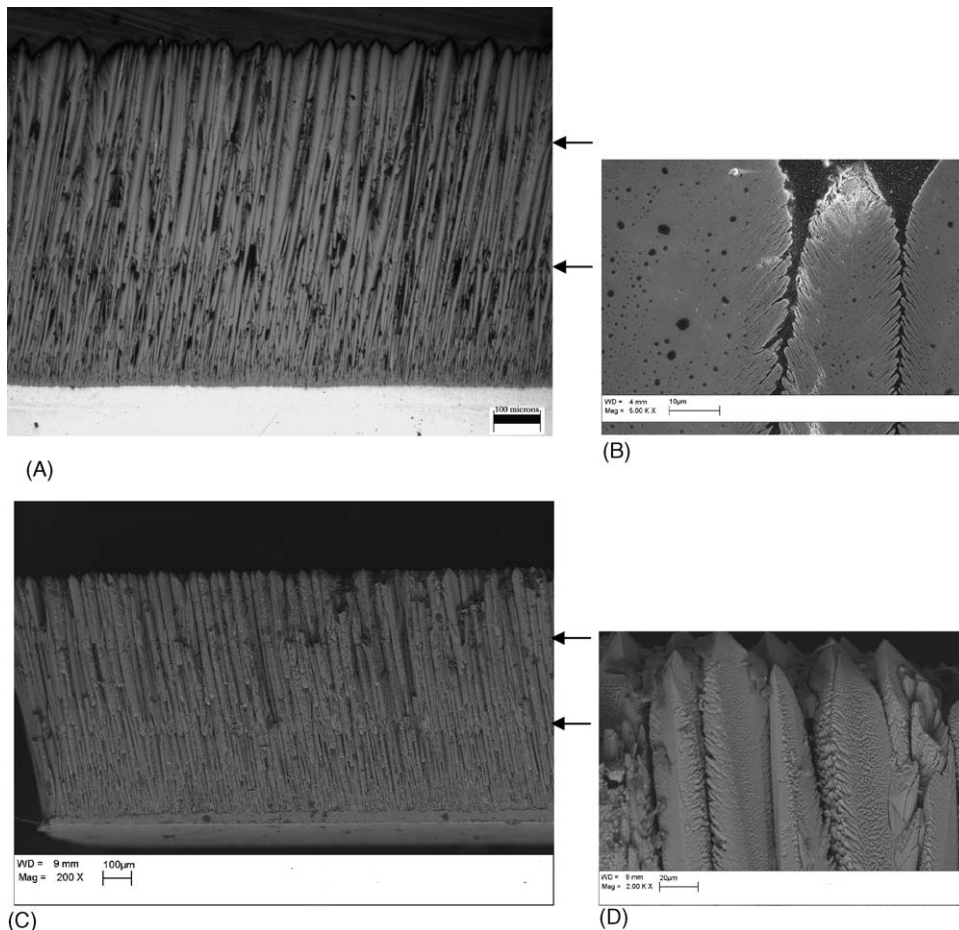


Fig. 2. Morphological features observed in an EB-PVD coating. (A) Polished micrograph showing columnar grains with large percentage of intercolumnar porosity. (B) High magnification SEM image showing features inside individual columns. (C and D) The corresponding fractured surfaces.

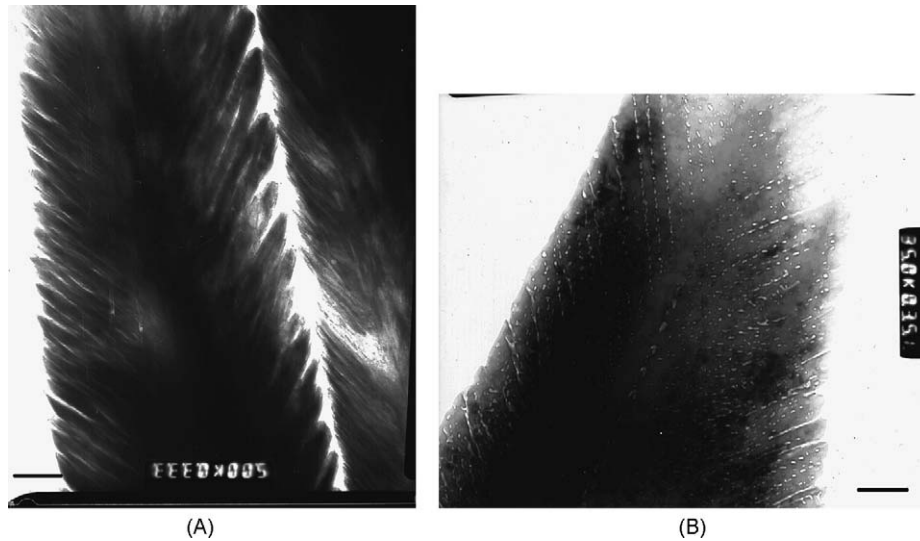


Fig. 3. Cross-sectional TEM micrographs revealing feathery cracks and fine pores inside each column. (A) Intercolumnar spacing along with feathery features are observed at the rim of each column, 5000 $\times$  magnification, the scale bar represents 2.5  $\mu\text{m}$ . (B) Feathery striations and intracolumnar fine voids are seen, 35,000 $\times$  magnification, the scale represents 200 nm.

non-transformable tetragonal structure as shown in Fig. 1. Also, it is seen that the processing conditions during deposition (deposition temperatures between 900 and 1100  $^{\circ}\text{C}$ , deposited normal to the stationary substrate plane) favor a dominant (200) texture of the nucleating columns [12]. The morphological features observed in these coatings, both in a polished cross-section and at fracture surfaces, are shown in Fig. 2. The coatings reveal a unique columnar morphology with 20–25  $\mu\text{m}$  wide crystals, growing perpendicular to the substrate plane, resulting in substantial intercolumnar porosity (1–5  $\mu\text{m}$  wide). The figures indicate that the porosity increases from a minimum near the bond coat interface to a maximum at the top of the coating. Porosity variations are not monotonic but rather exhibit local maxima in this case. This is typically not the case when the EB-PVD coatings are thinly deposited ( $\sim 250 \mu\text{m}$ ). However, in this present study, these local variations are attributed to the fact that the microstructure development of the coating was interrupted three times during deposition, as evident in Fig. 2A and C denoted by arrows. The coating in the present study was more thickly deposited thicker ( $\sim 800 \mu\text{m}$ ), particularly to achieve the required multiple neutron scattering in SANS studies. Also evident is the competitive growth closer to the substrate, where columns with dominant (200) crystallographic texture are favored to grow. Fig. 2B and D are high magnification SEM images of individual columns. The images reveal feather intracolumnar striations along with an extended size range of evenly distributed globular porosity in each column as a result of overshadowing effects and gas entrapment during deposition. Fig. 2D also reveals that the feathery striations grow inwards both from the facets of the columns and from the edges (as seen in the 2D images in Fig. 2B).

While micrometer size porosity is observed in SEM studies, the X-TEM studies carried out reveal microstructural features along different length scales (Fig. 3). A micrograph of an intercolumnar void at 5000 $\times$  magnification, Fig. 3A, indicates

feathery striations, which exist at the periphery of each column. These striations are oriented at 50–60 $^{\circ}$  to the substrate plane, consistent with the high magnification image observed under SEM (Fig. 2B). A higher resolution micrograph at 35,000 $\times$ , Fig. 3B, reveals strings of nanometer size pores inside a single column. The presence of nanosized intracolumnar pores is observed towards the center of the columns, at the inward tips of the feather cracks, and also towards the rim. These pores are a combination of globular and elongated spheroids, and range in size from 18 to 25 nm, as determined from image analysis. While important information on the nature of the porosity is obtained from SEM and TEM, advanced techniques, discussed further, complement this information by quantifying the features.

Coating characterization in terms of the porosity from MIP and precision density, the thermal conductivity and the elastic modulus are discussed below. The surface-connected porosity, measured using MIP, is in close agreement with the total porosity measured using the PD technique. This suggests that most of the porosity in this case is open and interconnected porosity (intercolumnar pores, intracolumnar striations and globular pores connected to the feathers). The thermal conductivity and elastic modulus behavior of these coatings is significantly different from those of APS coatings. The thermal conductivity of the EB-PVD coating measured 1.9 W/m K, which is high compared to that for an APS coating (1 W/m K) [18] (Table 1). This is due to the very different pore architectures in the two coatings. While APS coatings have predominantly a layered porosity, the

Table 1  
Coating properties with standard deviations

MIP porosity (%)	20 $\pm$ 2
Precision density porosity (%)	21.75 $\pm$ 1.45
Thermal conductivity (W/m K)	1.9 $\pm$ 0.13

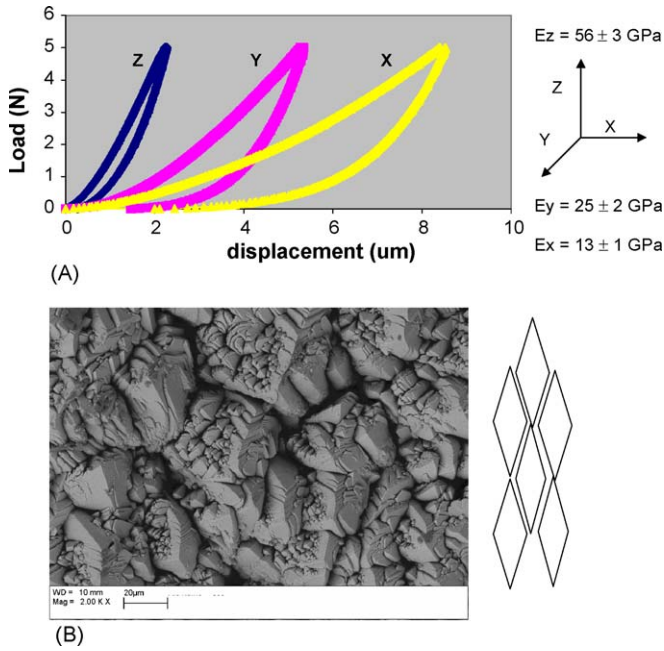


Fig. 4. (A) Depth-sensitive indentation behavior of EB-PVD coating in two in-plane (X and Y) and out-of-plane (Z) directions and (B) microstructural features observed on the top surface.

majority of the porosity in the EB-PVD case are intercolumnar pores, which are vertical to the substrate plane, thus providing less resistance to heat flow. Also, due to the nature of the deposition process (vapor condensation), the columns grow in an intrinsically homogeneous fashion (without either the microcracks seen in APS or grain boundaries). The elastic modulus measurements were carried out both out-of-plane and two in-plane directions, as shown in Fig. 4, to verify the anisotropy. Fig. 4A shows the load–displacement behavior for the three directions along with the elastic modulus values. While the coating is stiff in the out-of-plane (through thickness) direction, the depth of penetration is larger in the in-plane (cross-sectional) directions; hence the elastic modulus is significantly higher in the out-of-plane direction ( $56 \pm 3$  GPa). However, due to the intrinsic nature of the coating microstructural development (competitive growth among crystal nuclei by vapor condensation), a different scale of anisotropy is observed. The coating microstructure displays property anisotropy in three directions. The anisotropy in elastic modulus can be explained by study of Fig. 4B, looking at the top surface of the coating. It is evident that the columns grow in an elongated diamond shape, thus introducing anisotropy in the two in-plane directions, as well as between these and the out-of-plane direction.

Table 2  
Quantitative MSANS model results

Void component	Porosity (%)	Surface area ( $\text{m}^2/\text{cm}^3$ )	Mean opening dimension, (OD) ( $\mu\text{m}$ )	Mean pore diameter ( $\mu\text{m}$ )
Intercolumnar pores, $\beta = 1/10$	$13.05 \pm 1.31$	$1.25 \pm 0.6$	$0.2145 \pm 0.005$	–
Intracolumnar cracks, $\beta = 1/10$	$5.65 \pm 0.56$	$5.42 \pm 0.27$	$0.0215 \pm 0.005$	–
Nanometer globular pores	$3.05 \pm 0.31$	$3.81 \pm 0.19$	–	$0.0480 \pm 0.01$
Total	$21.75 \pm 1.45$	$10.48 \pm 0.34$	N/A	N/A

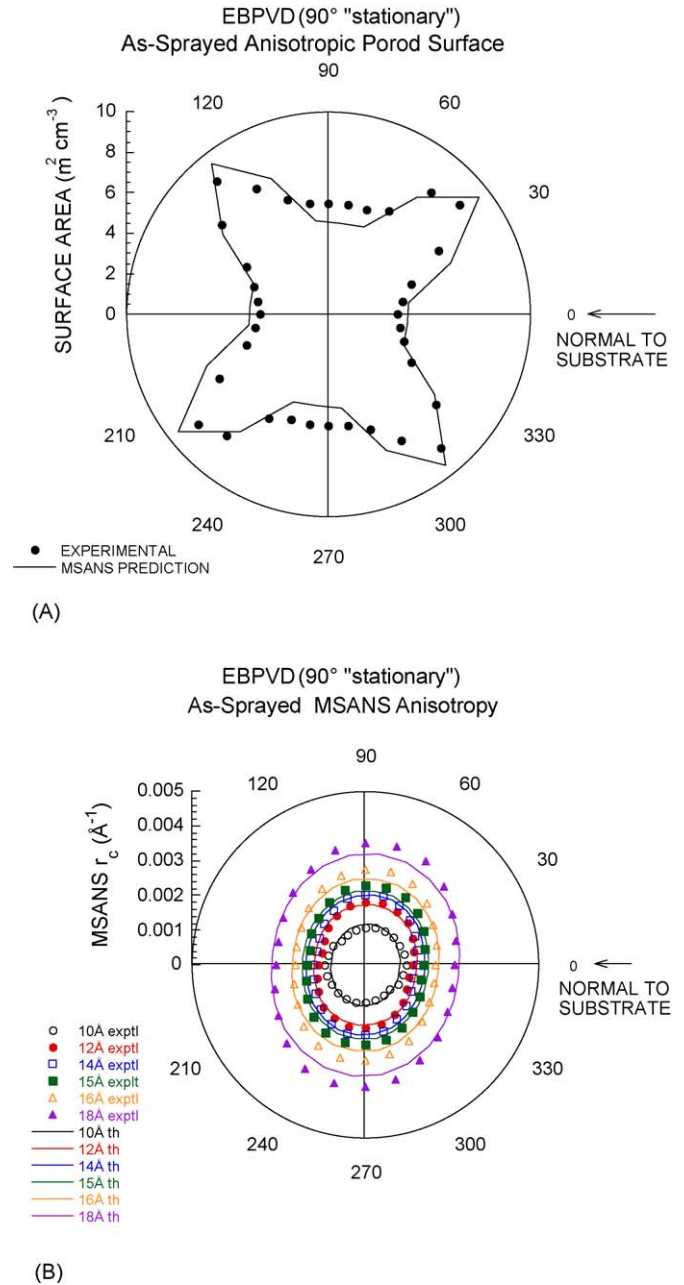


Fig. 5. Anisotropic Porod surface area and MSANS broadening experimental data (symbols) with model-fits (lines) for the EB-PVD coating (A) anisotropic Porod surface area; (B) anisotropic angular MSANS,  $r_c$ , at different wavelengths.

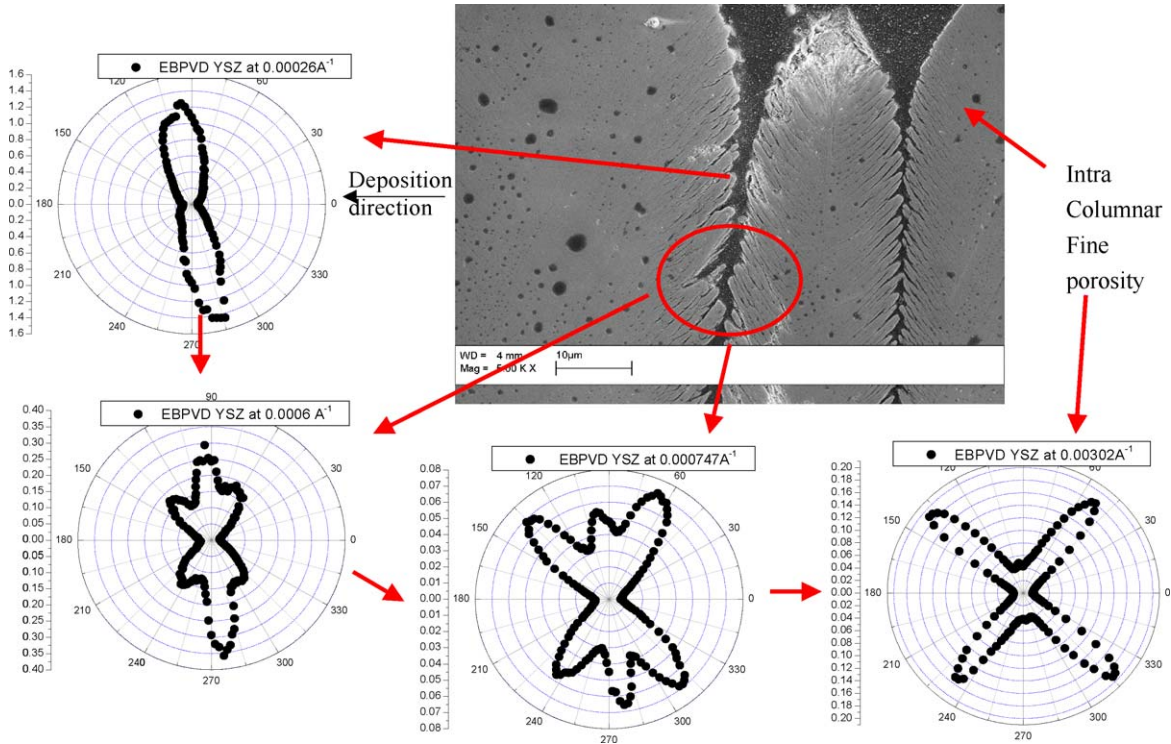


Fig. 6. Scattering intensity as a function of azimuthal angle  $\alpha$  for different values of  $Q$  compared to microstructural features observed. The errors are within the sizes of the data points.

3.1. SANS results

The SANS results along with the fit to the MSANS model include the component porosities of the interlamellar pores and intrasplat cracks, together with their mean opening dimensions and approximate orientation distributions, as well as the porosity of the globular pores and their mean diameter. The MSANS model is modified from that used for APS deposits [17] in that the three void model components have different orientations and sizes. Because axial symmetry may not be implicitly assumed for EB-PVD microstructures, especially after gaining input from elastic modulus measurements, the anisotropic Porod scattering was measured for two sample orientations, i.e., with the incident beam both out-of-plane and in-plane. However, the total surface area,  $S_T$ , has been estimated by calculating the “axially symmetric” 3D average from the in-plane orientation Porod scattering ( $6.06 \pm 0.35$ )  $m^2/cm^3$ , then multiplying this by the ratio of the 2D-average Porod surface found for the out-of-plane ( $9.92 \pm 0.84$ )  $m^2/cm^3$ , divided by the apparent Porod surface area projection at  $90^\circ$  for the in-plane orientation ( $5.47 \pm 0.34$ )  $m^2/cm^3$ . To model the intracolumnar cracks and intercolumnar pores, these are assumed to consist of separate networks of oblate spheroidal elements with aspect ratio values of 1/10. From microscopy, it is observed that the intracolumnar cracks are V-shaped with planar pore normals predominantly making an angle to the substrate normal in the middle angular range  $30\text{--}60^\circ$ . Intercolumnar pores are mainly parallel to the columns, i.e. perpendicular to the substrate and therefore in the high  $60\text{--}90^\circ$  angular range. The total porosity ( $21.75 \pm 0.10$ )%, determined by PD, and,

$S_T$  from the Porod data were used as input for the MSANS model.

Fig. 5 shows the experimentally deduced Porod surface area and MSANS anisotropy compared with the model predictions. The apparent anisotropic surface area distribution, derived from the anisotropic Porod scattering, Fig. 5A, amplifies the actual surface area orientation dependence of the scatterers. It is observed that the major contributors to the surface area are the intracolumnar pores and fine globular porosity. Fig. 5B shows the anisotropic angular variation of MSANS  $r_c$  at different

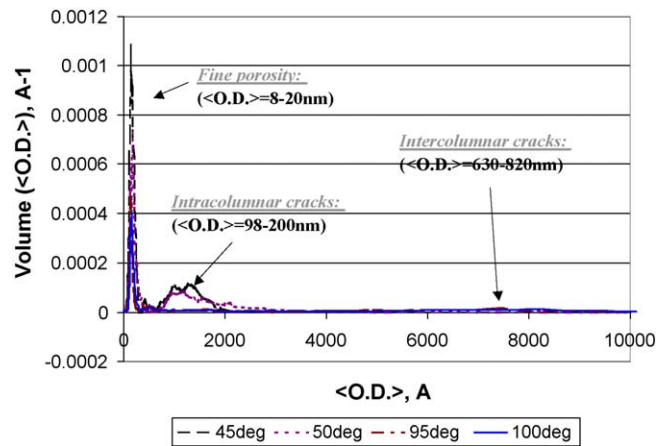


Fig. 7. MaxEnt volume-fraction size distributions of the EB-PVD coating, for different orientations of  $Q$  with respect to the deposition direction. The angle is defined as that between  $Q$  and the substrate normal. The figure shows three sizes consistent with the observed microscopy results.

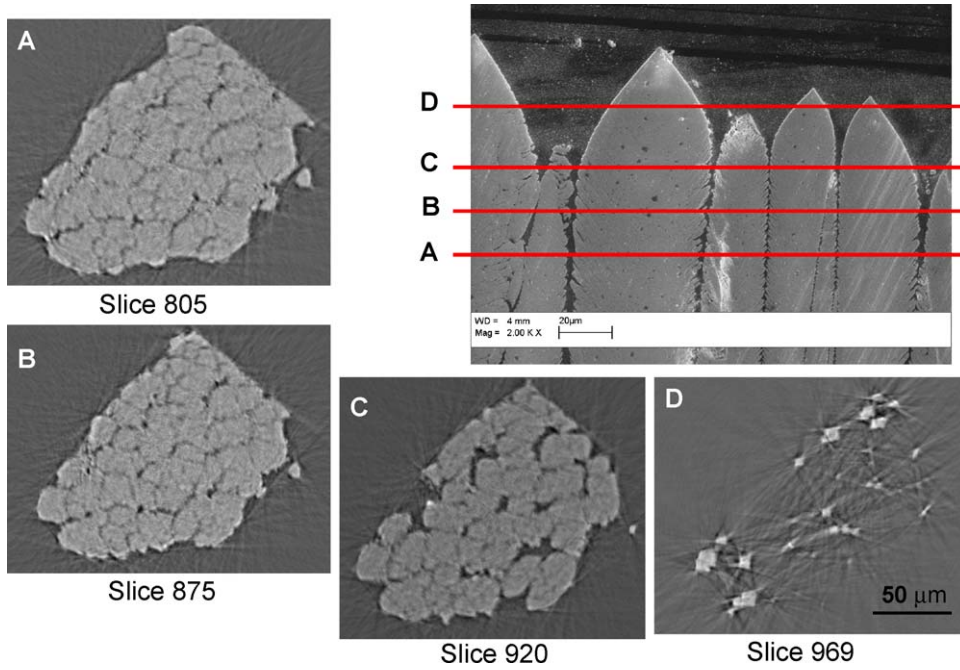


Fig. 8. Reconstructed sections, indicated on the micrograph showing variation in intercolumnar spacing with thickness. Figure shows the columnar spacing increasing towards the top of the coating and (D) shows tip of columns.

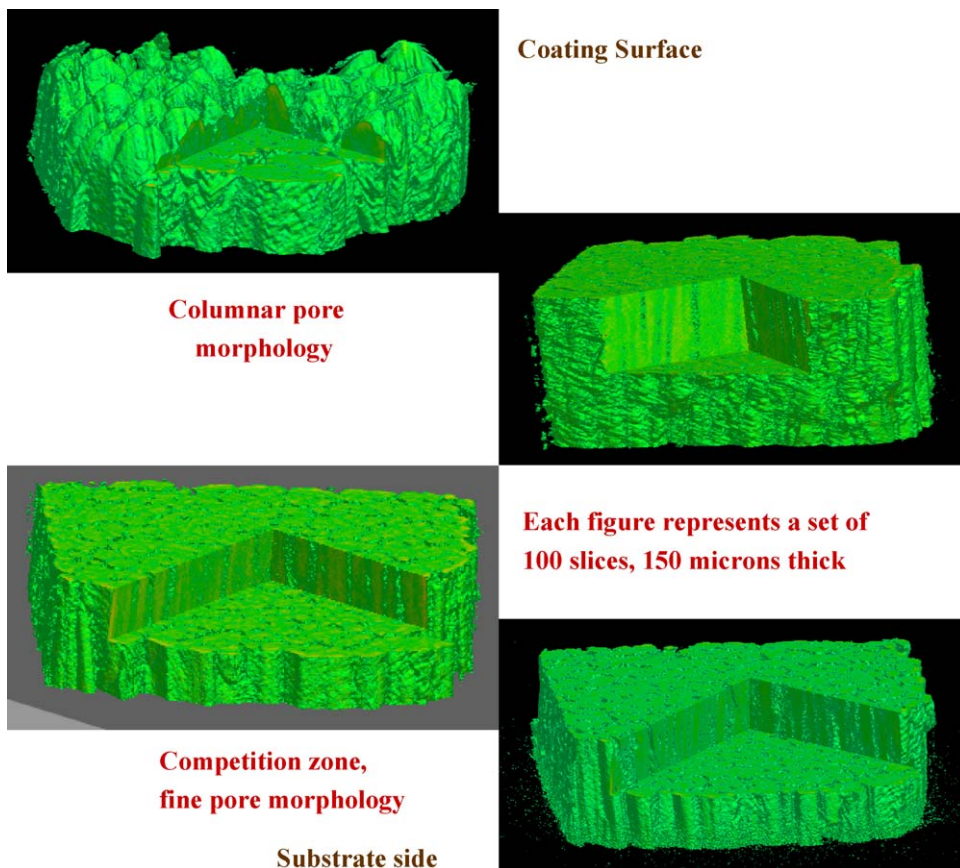


Fig. 9. Pore morphology in EB-PVD TBCs in 3D, showing fine porosity in the competitive zone near the substrate and intercolumnar pores at 1.3 μm resolution.

wavelengths in the plane of the coating cross-section. The dominant coarse scatters are the intercolumnar pores in the system, shown in Fig. 2A. After satisfying all the constraints in the MSANS model, the results for porosity contributions and mean opening dimensions are summarized in Table 2. The quantitative separation of the coating microstructure into its components, obtained from the MSANS model, shows that the intercolumnar pores contribute the most to the total porosity (60%) followed by intracolumnar cracks (26%). The globular pores contribute the remaining porosity.

### 3.2. USAXS results

A summary of some of the USAXS studies of the EB-PVD coating is presented in Fig. 6. The anisotropies in the scattered intensity at different  $Q$  values are presented as a function of azimuthal angle with respect to the substrate-normal direction. Also indicated are the features in the microstructure to which the scattering anisotropies can be attributed at each of the various length scales interrogated. The mean size of scatterers contributing at any  $Q$  is inversely proportional to the  $Q$  values (Bragg's law). The largest scatters (intercolumnar pores) scatter at the smallest  $Q$ , followed by the feathery striations at intermediate  $Q$  and the nanosized fine pores at the largest  $Q$  values. The combination of scattering data collected as a function of  $Q$  for each orientation and as a function of orientation at a particular  $Q$  provides quantitative information on the void microstructure within the coating as a function of void size. Fig. 7 presents apparent volume-fraction size distributions derived from the calibrated USAXS intensity versus  $Q$  using the maximum entropy size distribution routine, MaxEnt [25,26]. The MaxEnt analysis gives apparent size distributions that vary for different orientations of  $Q$  with respect to the substrate normal. This is because anisotropic orientation distributions are not taken into account here. A more comprehensive anisotropic model is being developed for the analysis of USAXS measurements made with multiple sample orientations. However, depending on the void

shapes assumed, MaxEnt can be used to provide a rough estimate of the void sizes present. Thus, Fig. 7 shows the different feature sizes that dominate the anisotropy at different magnitudes of  $Q$ . The results reveal a hierarchy of pores of at least three sizes broadly consistent with the SEM microstructures observed. A mean void dimension between 630 and 820 nm is indicated for the intercolumnar pores, while that for the intracolumnar feathery cracks lies between 100 and 200 nm. The nanometer globular pores exhibit diameters between 8 and 20 nm. However, it should be noted that the  $Q$  range of the USAXS instrument enables measurements of void sizes below  $\sim 1.5 \mu\text{m}$  in diameter.

### 3.3. XMT results

XMT studies were carried out to image the 3D columnar structure non-destructively. The raw data collected as cross-sectional X-ray attenuation maps are normalized and reconstructed using the filtered backprojection algorithm to generate 2D slices. Fig. 8 shows four such reconstructed images of individual slices along the thickness of the coating along with an SEM micrograph. The figure shows the change in intercolumnar spacing through the coating thickness. Also seen are the tips of the columns in one projection. These 2D slices are volume rendered to generate 3D projections. Fig. 9 shows the microstructural features in the EB-PVD coating in a 3D representation where the void space is displayed as transparent. A fine porosity is revealed in the competition zone near the substrate, where columns of all crystallographic orientations nucleate and then the dominant orientation favored by the deposition conditions in the chamber grow further. The columns are seen along with intercolumnar pores to extend through the thickness of the coating. The quantitative analysis for porosity information and gradient with thickness involves the following procedure: (a) generation of a histogram of the linear attenuation coefficient from the gray scale images. These show bimodal peaks, one due to the voids and the other due to solid material, (b) selection of region-of-interests in individual images, and (c) conversion

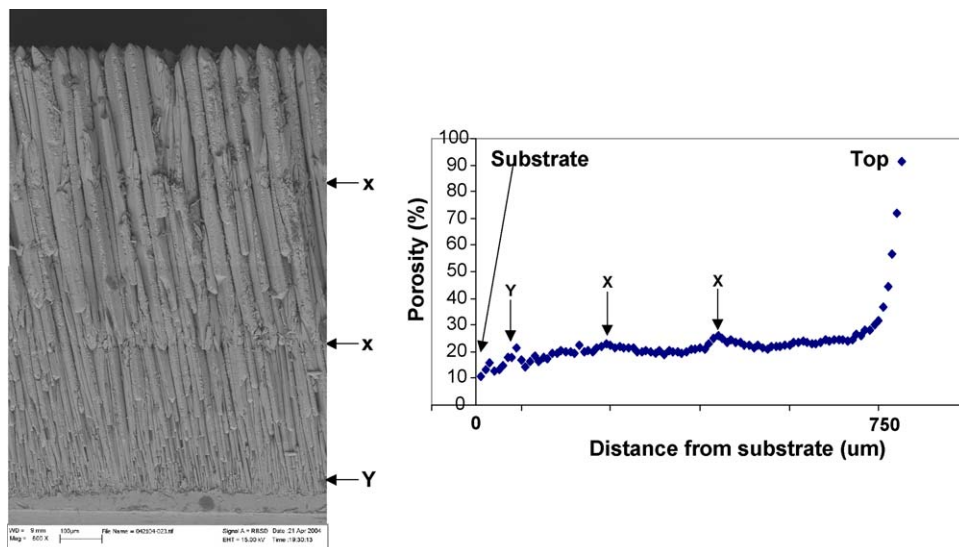


Fig. 10. The porosity gradient through the thickness of the coating in a fractured cross-section micrograph as well as the XMT studies. The X denotes the interface between successive deposition layers whereas the Y denotes the substrate coating interface.

of the gray scale density maps to “Black and White” images by a process of segmentation involving population assignment (materials and pores) for each voxel. Since the pore/grain boundary in the image is fuzzy due to finite voxel resolution and data collection noise, a localized thresholding procedure based on indicator kriging [24] is used. More detailed analysis of this procedure is presented elsewhere [27]. Porosity measurements are done by voxel counting of black and white regions in the segmented images.

Fig. 10 depicts the porosity gradient through the thickness of the coating in a fractured cross-section micrograph derived from the XMT studies. Each individual point in the figure is a volumetric average of 10 slices in the coating. Also the standard deviation for each point is about 1–2%, which is unnoticeable on the graph. A variation in microstructure and texture is anticipated throughout the thickness of the coating due to the competitive nature of the growth process. The results reveal the presence of a high porosity region in the competition zone near the substrate (marked as Y in the figure), where columns of several crystallographic orientations nucleate. Columns with preferred orientation, depending on the deposition conditions in the chamber, grow beyond this point, thus showing another increase in porosity (or intercolumnar spacing) towards the top surface of the coating. Porosity variations are not monotonic but rather exhibit local maxima, as shown in Fig. 2C and marked as X in Fig. 10. These local variations arise from interruptions in the deposition process. A sharp increase in porosity towards the coating top surface can be associated with the tapered column tips.

#### 4. Conclusions

Through a multidisciplinary approach combining conventional microscopy and advanced scientific tools (SANS (MSANS), USAXS and XMT), the quantitative relationships between the different components of the EB-PVD void microstructure have been successfully determined, providing new insights that will support future EB-PVD TBC design. Quantitative information on the distributions of various void defects, size, anisotropy and porosity gradient through the coating thickness has been obtained and is well complemented with 3D pore visualization by this integrated approach. These results are correlated with thermal conductivity and elastic modulus measurements, the properties most sensitive to these microstructural features. It is observed that the thermal conductivity of an EB-PVD coating is twice that of APS coatings. The elastic modulus exhibits an interesting anisotropy in all three orientations in the coating. Studies are underway to extend this kind of integrated approach to tracing the evolution of microstructural and property changes upon service-encountered heating, thereby helping comprehend failure mechanisms in these coatings.

#### Acknowledgements

This research was supported by the National Science Foundation MRSEC program at the SUNY Stony Brook under the Grant No. DMR-0080021. This work utilized facilities supported in part by the National Science Foundation under Agree-

ment No. DMR-9986442. We acknowledge the support of the National Institute of Standards and Technology, U.S. Department of Commerce, in providing the neutron research facilities used in this work. The authors wish to thank Dr. Sanjay Sampath of SUNY Stony Brook for valuable discussions and Dr. Boualem Hammouda of the NIST Center for Neutron Research and Dr. Pete Jemian of the Advanced Photon Source for scientific and technical support. The UNICAT facility at the Advanced Photon Source (APS) is supported by the University of Illinois at Urbana-Champaign, Materials Research Laboratory (U.S. DOE, the State of Illinois-IBHE-HECA, and the NSF), the Oak Ridge National Laboratory (U.S. DOE under contract with UT-Battelle LLC), the National Institute of Standards and Technology (U.S. Department of Commerce) and UOPLLC. The APS is supported by the U.S. DOE, Basic Energy Sciences, Office of Science under contract No. W-31-109-ENG-38.

#### References

- [1] R.A. Miller, *Surf. Coat. Technol.* 30 (1987) 1.
- [2] J.T. DeMasi-Marcin, D.K. Gupta, *Surf. Coat. Technol.* 68/69 (1994) 1.
- [3] W.J. Brindley, R.A. Miller, *Adv. Mater. Process.* 8 (1989) 29.
- [4] S.M. Meier, D.K. Gupta, *J. Eng. Gas Turbines Power* 116 (1994) 250.
- [5] J.T. DeMasi-Marcin, K.D. Sheffler, S. Bose, *J. Eng. Gas Turbines Power* 112 (1990) 521.
- [6] W. Mannsmann, H.W. Grunling, *J. Phys.* IV 3 (1993) 903.
- [7] W.A. Nelson, R.M. Orenstein, *J. Thermal Spray Technol.* 6 (2) (1997) p176.
- [8] R. McPherson, *Thin Solid Films* 112 (1984) 89.
- [9] T.E. Strangman, *Thin Solid Films* 127 (1985) 93.
- [10] C.A. Johnson, J.A. Ruud, R. Bruce, D. Wortman, *Surf. Coat. Technol.* 108/109 (1998) 80.
- [11] P. Morrel, D.S. Rickerby, AGARD-R-823, paper 20, 1998.
- [12] J.A. Thornton, *J. Vac. Sci. Technol.* 12 (4) (1975) 830.
- [13] J.A. Thornton, *Ann. Rev. Mater. Sci.* 7 (1977) 239.
- [14] B.A. Movchan, A.V. Demchishin, *Fiz. Metal. Metalloved.* 28 (4) (1969) 83.
- [15] W.C. Oliver, G.M. Pharr, *J. Mater. Res.* 7 (1992) 1564.
- [16] J. Ilavsky, A.J. Allen, G.G. Long, S. Krueger, C.C. Berndt, H. Herman, *J. Am. Ceram. Soc* 80 (1997) 733.
- [17] A.J. Allen, J. Ilavsky, G.G. Long, J.S. Wallace, C.C. Berndt, H. Herman, *Acta Mater.* 49 (2001) 1661.
- [18] A. Kulkarni, Z. Wang, T. Nakamura, S. Sampath, A. Goland, H. Herman, A.J. Allen, G.G. Long, J. Frahm, R.W. Steinbrech, *Acta Mater.* 51 (9) (2003) 2457.
- [19] U. Bonse, M. Hart, *Appl. Phys. Lett.* 7 (1965) 238.
- [20] J. Ilavsky, A.J. Allen, G.G. Long, P.R. Jemian, *Rev. Sci. Instrum.* 73 (3) (2002) 1660.
- [21] Y. Wang, F. De Carlo, D. Mancini, I. McNulty, B. Tieman, J. Bresnahan, I. Foster, J. Insley, P. Lane, G. Laszewski, C. Kesselman, M. Su, Thiebaut, *Rev. Sci. Instrum.* 72 (4) (2001) 2062.
- [22] D. Mancini, F. DeCarlo, Y.S. Chu, B. Lai, *Rev. Sci. Instrum.* 73 (2002) 1550.
- [23] W.B. Lindquist, S.M. Lee, D.A. Coker, K.W. Jones, P. Spanne, *J. Geophys. Res.* 101 (B4) (1996) 8297.
- [24] W. Oh, W.B. Lindquist, *IEEE Trans. Pattern Anal. Mach. Intell.* 21 (1999) 590.
- [25] J.A. Potton, G.J. Daniell, B.D. Rainford, *J. Appl. Crystallogr.* 21 (1988) 663.
- [26] G.G. Long, S. Krueger, P.R. Jemian, D.R. Black, H.E. Burdette, J.P. Cline, R.A. Gerhardt, *J. Appl. Crystallogr.* 23 (1990) 535.
- [27] A. Kulkarni, H. Herman, F. DeCarlo, R. Subramanian, *Met. Mater. Trans. A* 35 (2004) 1945.